Construction and Building Materials 212 (2019) 486–499

Contents lists available at ScienceDirect

Construction and Building Materials

journal homepage: www.elsevier.com/locate/conbuildmat

Multi-scale observations of structure and chemical composition changes of portland cement systems during hydration

Masoud Moradian [a,*], Qinang Hu [a], Mohammed Aboustait [a], M. Tyler Ley [a], Jay C. Hanan [b], Xianghui Xiao [c], Volker Rose [c,d], Robert Winarski [d], George W. Scherer [e]

[a] Oklahoma State University, School of Civil and Environmental Engineering, Stillwater, OK 74078, USA
[b] Oklahoma State University, School of Mechanical and Aerospace Engineering, Tulsa, OK 74106, USA
[c] Argonne National Laboratory, Advanced Photon Source, Argonne, IL 60439, USA
[d] Argonne National Laboratory, Center for Nanoscale Materials, Argonne, IL 60439, USA
[e] Princeton University, Department of Civil & Environmental Engineering, Princeton, NJ 08544, USA

HIGHLIGHTS

- Non-uniform growth and dissolution were observed on the surface of particles.
- Hydration products with Ca/Si > 3 form on and near the particles before the acceleration period.
- Chemical composition of hydration products changed from the induction period to the acceleration period.

ARTICLE INFO

Article history:
Received 1 February 2019
Received in revised form 28 March 2019
Accepted 3 April 2019

Keywords:
X-ray Computed Tomography
Cement hydration
Acceleration period
Calorimetry
Induction period

ABSTRACT

There is little agreement about the mechanisms and few direct observations of the transition of cement paste from a slurry to a solid. This paper uses four different imaging techniques at multiple length scales (from 15.6 nm to 1 μm) to follow the three-dimensional microstructural evolution of portland cement, and monoclinic tricalcium silicate (mC_3S) paste over the first 16 h of hydration. Measurements of over 60,000 particles captured every 10 min were made at the micron scale. Nanoscale examinations of the structure and chemical composition are used to support this work. The results show that hydration products with an average Ca/Si > 3 form on and near the surface of the hydrating particles prior to the acceleration period that appears to control the reaction rate. These hydration products appear to change in chemical composition as more rapid dissolution of C_3S and formation of hydration products occur during the acceleration period. The findings are used to provide insights into the origin of the induction and acceleration periods during hydration.

1. Introduction

Despite decades of study, there is no general agreement about the processes or mechanisms that govern the early age hydration of C_3S[1] or portland cement paste. Improved knowledge of this process would allow for better control over cementitious materials and improved use of both chemical and mineral admixtures. This would allow for improvements in the economy, constructability, and sustainability of concrete, the most commonly used building material in the world.

Several hypotheses have been proposed in the literature to explain the initial dissolution of cement particles and the subsequent formation of the microstructure. Some suggest that a hydrated layer forms at the particle surface that reduces the accessibility to the surrounding solution and then this material subsequently disappears [1–3]. More recent publications have focused on the localized formation of etch pits [4,5] or more uniform dissolution, depending on the calcium concentration in the solution [6]. Others hypothesize that early hydration products form within these etch pits, which slows the release of ions and controls the local dissolution of the anhydrous particle by covering the most reactive sites [7–9].

Previous work studying changes in the chemical composition of the solution during the first 4 h of hydration of C_3S with w/s from

* Corresponding author.
E-mail address: Masoud.Moradian@okstate.edu (M. Moradian).

[1] Conventional cement chemistry notation is used throughout this paper: C = CaO, S = SiO_2, H = H_2O.

https://doi.org/10.1016/j.conbuildmat.2019.04.013
0950-0618/

0.70 to 20 shows that the Si concentration, [Si], is low (between 1 μmol/L and 4.5 μmol/L for w/s = 0.70) while the Ca concentration in solution, [Ca], increases over time and reaches a maximum (≈1700 mg/L for w/s = 0.70) near the end of the induction period [10]. After reaching a maximum value, [Ca] begins to decrease and [Si] begins to increase slightly. At the same time, the heat given off by the reaction begins to increase [5,11,12]. It is not clear what causes this heat release but it has been proposed to be caused by rapid dissolution of C_3S [5,11,13]. Unfortunately, these measurements only examined the average ionic concentration in the solution and no information is obtained about the change in microstructure for these periods.

Many hydration studies use bulk measurements and so they cannot provide detailed information about the individual particles during the reactions. Some examples of these bulk measurement techniques include isothermal calorimetry, chemical shrinkage, pore solution analysis, quasi-elastic neutron scattering (QENS), and nuclear magnetic resonance (NMR) [13–22]. Imaging has been used to make complementary observations of the evolution of the microstructure over time. This is typically done with scanning electron microscopy (SEM) or transmission electron microscopy (TEM) after arresting hydration [23–26]. Hydration is typically stopped by using isopropyl alcohol or other solvents to remove the water through solvent exchange followed by drying [27–30]. The samples are then cast into epoxy and polished or fractured and a surface is investigated. This process has the potential to introduce artifacts [7,24,25,28,29,31]. If an in-situ technique could be used to study this process then more insights might be gained.

One important study used a single particle of C_3S with w/s = 2. Hydration was arrested on three different samples with acetone after 5, 30, and 60 min [31]. The selected times corresponded to the initial reaction, the induction period, and the onset of the acceleration period in the calorimetry curve. After arresting hydration, the sample was broken and investigated by SEM. The authors observed a non-uniform layer of hydration product around the original particle which grew in thickness in the induction period and then shrank at the onset of the acceleration period. Poorly crystallized CH precipitates were observed at the end of the induction period that dissipated during the acceleration period. This observation complements other publications suggesting that the formation of CH is an important feature of the transition from the induction period to the acceleration period [12,32,33]. The suggestions of the CH forming during the acceleration period and then dissipating was first introduced in [31]. This important observation is rarely discussed in the literature, perhaps because the image quality was poor, there was no chemical analysis to support their claims, and there may have been concerns over the high w/s and the use of acetone to arrest hydration.

Juenger et al. used soft X-ray transmission imaging to collect time-lapse transmission images while C_3S reacted at w/s = 5 [34]. These images suggest that the hydration process is not limited to the surface of the C_3S particle and can occur inside the particle as well. However, if the transmission path of the X-rays is too long (>10 μm for anhydrous C_3S), then there will be insufficient transmission of X-rays and so no images can be produced. Higher energy X-ray imaging techniques, such as laboratory and synchrotron X-ray Computed Tomography (XCT) allow for more than an order of magnitude higher penetration. This can allow the 3D microstructural data to be obtained non-destructively from the micron to nanometer length scale [35–43].

Recent work has combined nano-tomography and nano-X-ray fluorescence in a technique called nano-tomography assisted chemical correlation (nTACCo) to capture quantitative measurements of 3D structure, chemical composition, and mass density of the hydration products. This method has been used to observe early particle dissolution and subsequent hydration product growth with a resolution of 50 nm [44,45]. These experiments reveal changes in structure and chemical composition, but have not been performed continuously.

More in-situ observations are needed of cement particles as they react at relevant w/s. However, the acquisition time for typical XCT is several hours and there will be artifacts created if there is movement. Because of this, XCT is a challenging technique to use to study in-situ early age hydration reactions and often requires the reactions to be first arrested in order to be studied [46,47]. Fortunately, recent developments in fast data acquisition rates from high-flux synchrotron sources have made it possible to collect 3D data at the micron scale in a few seconds [46–51]. This technique is named fast computed tomography (fCT). This reduction in acquisition time makes this technique useful for studying early cement hydration.

In this paper, four different types of imaging techniques are used to study hydration of portland cement related powders at different length scales. These include fCT and Nano Computed Tomography (nCT) at multiple length scales. In addition, SEM with Energy-Dispersive X-ray Spectroscopy (EDS) and Nano X-ray Fluorescence (nXRF) were used to evaluate compositional changes of some samples before and after hydration. The focus of this work is to find greater insights into the mechanisms that control the change from the induction to the acceleration period in both portland cement and C_3S hydration.

2. Method and experiment

2.1. Materials

Cementitious materials used for the tests were NIST cement number 168 from the Cement and Concrete Reference Laboratory (Frederick, Maryland) (OPC) [52], and monoclinic C_3S (mC_3S). The mC_3S samples were produced by Mineral Research Processing (Meyzieu, France). These materials were investigated by XRF, automated scanning electron microscopy (ASEM), XRD analysis, isothermal calorimetry, and Blaine fineness (ASTM C204).

The specifications and bulk chemical composition of the investigated materials are presented in Table 1. The experimental details of ASEM are included in other publications and the Appendix [38,53]. According to ASEM and Blaine fineness, OPC was slightly finer than mC_3S.

XRD analysis demonstrates that mC_3S powder is close to pure C_3S. XRD analysis of OPC powder can be found in another publication [52]. The heat release measurements were conducted by a Tam Air Isothermal Calorimeter at a constant temperature of 25 °C, and the hydration rate was monitored for 24 h. More detail about this test can be found in the Appendix.

2.2. Examination of pastes

2.2.1. Sample preparation and instruments setting

Four paste samples were examined at different w/s with a pixel size of 1 μm/voxel with fCT as reported in Table 2. Two different w/s (one lower and one higher) were used for each powder because it was important to make a sample that was well compacted and to investigate the differences in performance. The technique was able to collect a tomograph in less than 5 s. Each tomograph was a cylinder that was 2016 μm wide and 1536 μm tall. These experiments were conducted at beamline 2-BM at the Advanced Photon Source (APS) at Argonne National Laboratory. This is possible because of advancements in detector design and high photon flux. More details about the facility and reconstruction can be found in other publications and the Appendix [50,51]. Since each scan was only 5 s in length, this means that each sample was only exposed

Table 1
Specifications and chemical composition of binders.

	Blaine (cm^2/gr)	Density (gr/cm^3)	Mass composition (%)						Phase concentration (%)			
			SiO_2	CaO	Al_2O_3	MgO	Fe_2O_3	SO_3	C_3S	C_2S	C_3A	C_4AF
OPC	3790	3.15	19.91	62.27	5.11	3.87	2.15	3.49	54.5	15.7	8.0	7.0
mC_3S	3588	3.12	26.54	71.97	0.94	0.06	0.48	–	~100	–	–	–

Table 2
Properties of fCT and calorimetry samples and scan times for fCT test.

Cementitious material	w/s	Time for the first tomograph (hours: minutes)	Time for the last tomograph (hours: minutes)
mC_3S	0.70	1:10	15:40
mC_3S	0.45	1:10	15:40
OPC	0.60	0:34	11:34
OPC	0.40	0:34	11:34
mC_3S powder	–	–	–
OPC powder	–	–	–

to the X-ray radiation for ≈ 7.5 min over roughly 15 h, so the damage from X-ray radiation is expected to be negligible. This is supported by other work done with the same instrument to investigate inorganic materials [54]. Samples were prepared with 5 g of powder and the necessary water to reach the desired w/s. Water was added to the cementitious powder, and the mixture was stirred 10 times clockwise and 10 times counterclockwise in a vial by a stainless steel rod. Then the vial was placed in a Vortex Mixer produced by Stuart (Staffordshire, UK) and mixed with a speed of 1000 rpm for three minutes. The same procedure was used for the calorimetry test but 3 g of powder was used. More detail about mixing and sample preparation are discussed in the Appendix. Dry powders were also investigated to aid in the segmentation of the data sets. This will be discussed in Section 2.2.3.

2.2.2. Overview of fCT and XCT

Sample alignment took between 34 and 70 min. After alignment, 3D tomographs were collected every 10 min. Fig. 1 shows the 3D tomograph and a typical slice from the mC_3S sample with w/s = 0.70. The gray values in the XCT and fCT datasets correlate to the X-ray absorption of the material. Therefore, a change in gray value for a given location could be attributed to the difference in chemical composition, density, or both. These gray values allow the data to be separated into different constituents and then quantitatively evaluated. This process is called segmentation. A segmented or binary image showing the material with high X-ray absorption is shown in the lower right of Fig. 1. The steps used to create this image will be discussed in the next section and the Appendix.

2.2.3. Image processing

First, a median filter (radius of 2.5 μm) was used to remove noise. Next, ranges of gray values were chosen to separate the different materials for data processing. To help guide this decision, the dry powder was scanned and the bulk density was measured. By using the bulk density and the volume of the container, the volume of the powder was calculated. Once the volume of powder was known, different threshold values were chosen and the volume was estimated and compared to the calculated volume of powder. This threshold level was used to determine the gray value that indicates the anhydrous material. The anhydrous material and all hydration products with similar X-ray absorption will be known as high absorption material for this work. The calculated threshold value was applied to all collected tomographs and the single voxel regions were removed from the data as they are at the spatial limit of the method and so could not be investigated reliably.

Because there was not a clear difference in the gray values of the different materials, it was decided to separate the data into low and high X-ray absorption material due to the high X-ray energy level in fCT measurements. The low-absorption material consists of voids, water-filled space, mixtures of water and submicron anhydrous particles, and low-density hydration products. The high-absorption material consists of everything else, including anhydrous cement and some hydration products close to the surface of the anhydrous cement grains with an X-ray absorption similar to or higher than the original reactant.

A limited region of the sample that is 1000 μm in diameter by 100 μm in height was used for the analysis. This region was used to reduce the computational expense and also to avoid beam hardening artifacts that may occur near the edges. This allowed over 60,000 particles to be investigated from each sample in the region of interest. The same settings were then used to segment the high-absorption material in the slurry scans. Fig. 1 shows a region of a cross section before and after the segmentation of high-absorption materials.

The slurry samples contain water, but this should have minimal impact on the measured gray values, as water has a low X-ray absorption. In medical CT scans it is common to use a fixed range of gray values for segmentation regardless of the surrounding fluid [55]. The sensitivity of the results of the segmentation was investigated by altering the segmentation values by ±2.5% of the calculated threshold value. These differences were chosen based on the expected variation that may occur from the bulk density calculation of the powder. Over this range of values, the same trends were observed and the magnitudes only slightly changed. Therefore, the selected segmentation method seems reliable. More details about segmentation and quantification can be found in the Appendix.

2.3. Examination of individual particles

A collection of individual particles was investigated with other imaging techniques at higher resolutions to complement the fCT data. Because of the high resolution of these techniques, only a few microns of a sample could be scanned. In addition, the source energy of the instruments is low at nano scale resolutions and so the samples have to be small enough to obtain high-quality data. These explain why individual particles (and not paste) were hydrated and examined for this section. These particles were epoxied to the end of a graphite rod and then allowed to react in higher w/s solutions. These more dilute solutions were used to allow for imaging. The reaction of cement particles in dilute solutions is rapid because of the undersaturation of the solution surrounding the particles [56]. To address this, the particles were immersed in 15 mM lime or saturated lime + gypsum solutions. These solutions were shown to have heat evolution curves comparable to suspensions with w/s from 0.5 up to 5.0 [1,56]. SO_4 ions were used in this solution as it is more representative of the pore solution in portland cement. nCT was used to investigate the microstructural change of the reacting particles, while SEM/EDS and nXRF were conducted to obtain chemical information from individual particles.

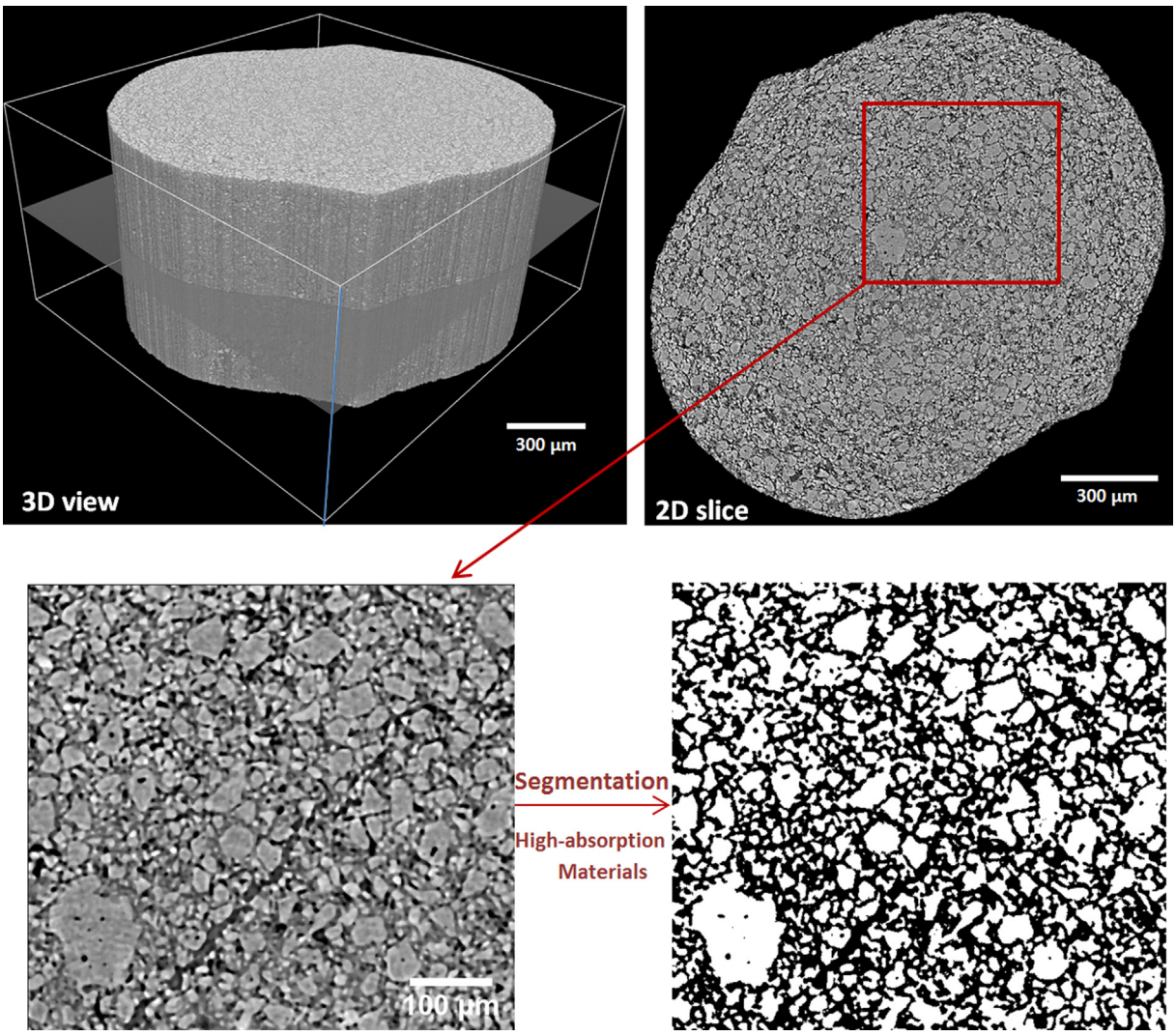

Fig. 1. Examples of the 3D reconstruction, a 2D slice, and a region before and after segmentation of high-absorption materials from mC_3S paste with w/s = 0.70.

2.3.1. nCT

A 3D tomograph was acquired at nanoscale resolution both before and after a certain period of reaction. The measurements were made using an UltraXRM-200 with an X-ray energy 8.3 keV at a voxel size of 130 nm and with an Ultra 810 with an X-ray energy of 5.3 keV at 65 nm and 15 nm/voxel. The details of the instruments can be found in the Appendix. The lower X-ray energy levels of these imaging methods provide higher contrast to the X-ray absorption of the hydration products. This gives more insights into the hydration products that might not be detected with the higher energy imaging methods, such as fCT.

Two samples with a collection of particles on the tip of a graphite rod were investigated for hydration periods of 2 h and 10 h with w/s = 5 in a solution saturated with lime + gypsum. The schematic of the test setup is shown in the Appendix. Both samples were imaged before and after the reaction to compare their changes relative to their initial state. After the initial scan, the sample was placed in a N_2 environment and then added to a sealed cell for the reaction. The cell was stored in the N_2 environment to protect it from carbonation as it hydrated. The reactions were then arrested by 99% isopropyl alcohol after the desired time of hydration and the sample was scanned again with nCT.

A computer algorithm for 3D image registration was created to align the two scans [37,44]. A qualitative segmentation of the anhydrous C_3S and hydration product was completed by choosing gray values that adequately separated the materials and minimized background noise. The threshold values for anhydrous C_3S were chosen to match the border of the sample as found by the nXRF scans. Since the nXRF shows the high contrast between air and solid material, this was useful to compare the data sets. This method has been successfully used in the past [45].

2.3.2. Changes in chemical composition

2.3.2.1. nXRF and nTACCo. The chemical composition of the reacted particles in nCT was investigated with nXRF. In this technique, a primary X-ray beam illuminates the sample and X-ray fluorescence radiation leaving the sample is detected by a four-element silicon drift diode detector that is perpendicular to the X-ray beam direction (Vortex ME4) [57]. The measurements were conducted with an X-ray spot size smaller than 50 nm at the hard X-ray nanoprobe beamline at sector ID-26 of the Advanced Photon Source (APS) and the Center of Nanoscale Materials (CNM) at Argonne National Laboratory. Details about calibration and analysis can be found in the Appendix and in other publications [44,57].

Nano-tomography assisted chemical correlation (nTACCo) is a technique that combines nCT and nXRF data. By fusing the 3D structural information into the 2D chemical mapping, the elemental density (g/cm^3) can be measured for intermixed phases at the

nanometer length scale. The details of this procedure are given in previous publications and the Appendix [37,44,45].

2.3.2.2. SEM/EDS. To learn more about the changes in the surface chemical composition, OPC and mC_3S particles were examined by SEM/EDS analysis in the same orientations and locations before and after being placed in dilute 15 mM lime solution with w/s = 10 and then subsequently in isopropyl alcohol. A typical sample can be seen in the Appendix.

Since the goal of this work was to investigate the changes in the surface chemical composition at known locations, no sample preparation or surface coatings were used. Previous work has shown that this method of investigation showed agreement with nXRF of hydration products and so a validation of the procedure is not presented [45].

For this analysis, several samples were investigated before and after hydration for OPC and mC_3S. The samples were carefully aligned after reaction so that the same orientation and locations were investigated. Different samples were investigated after 5 min, 10 min, 20 min, and 36 min of hydration in 15 mM lime solution with w/s = 10. Points were only investigated if the Ca/Si was less than 4. This is done to exclude points that are likely to be CH.

3. Results

3.1. Paste samples

3.1.1. Changes in high-absorption material

Fig. 2 illustrates the changes of the volume of high-absorption materials during hydration. These measurements are based on the volume of more than 60,000 particles. Since it took time to align the samples, there are no tomography data for the early age hydration of the pastes.

In all samples, the volume of the high-absorption materials increased to a maximum value and then decreased and did not change. The initial increase was not observed in mC_3S with w/s = 0.45; however, the peak could have occurred prior to the first tomograph at 70 min. For all samples, the volume of high-absorption material is higher than the estimated volume of the anhydrous powder at the time of mixing. This observation will be discussed in detail throughout the paper. The increase was higher for pastes with higher w/s.

The shape of the curve is similar for all four samples. This reproducible behavior by different samples and materials is not likely to be an artifact. Instead, the maximum appears to be a real event in the hydration of both mC_3S in calcium + gypsum solution and portland cement. This seems to be the formation of high X-ray absorption hydration product that then changes to hydration product with a lower absorption. Furthermore, the observed changes are several times higher than the variation after ≈ 5 h when the data are not changing. This suggests that these changes observed in the first ≈ 5 h of hydration are significant.

To examine the sensitivity of these measurements to the segmentation method, the gray value thresholds for mC_3S paste with w/s = 0.70 were varied by ±2.5%. While the changes in the threshold value did affect the magnitude of the measured values, they do not change the trend and timing of the curves. Therefore, the segmentation procedure seems to be robust enough for the conclusions drawn. The details of this analysis can be found in the Appendix.

Fig. 3 shows the isothermal calorimetry and the percentage of high-absorption material on the same plot. Since the preparation of the paste samples for fCT uses the same mixing procedure as the calorimetry experiment, the results from two different experiments should be comparable and provide insight into correlations between the microstructural changes and the rate of reaction.

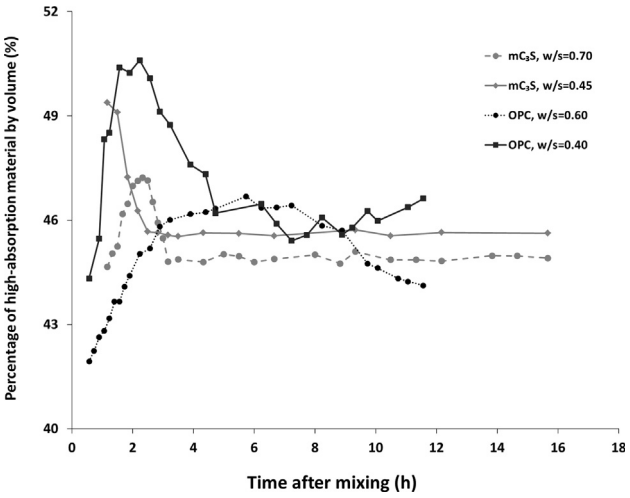

Fig. 2. Volume change of high-absorption material versus time after mixing.

The increase in the high-absorption material appears to occur during the induction period. Others have suggested that hydration products begin forming as soon as the solution is introduced to anhydrous particles [10,12,31]. If these hydration products form on the surface of the original high-absorption material then this could explain why the material is observed to increase in size.

The decrease in the high-absorption material occurs at the beginning of the acceleration period, except in OPC with w/s = 0.6, which could occur if the products are not stable or if the local solution chemical composition changes enough to cause these hydration products to dissolve or transform to another phase with different chemical composition. The high-absorption material stays almost constant in volume as the acceleration period continues; however, the calorimetry curves suggest the rates of reaction are still high. The OPC system has a greater volume increase and heat release than the mC_3S powder. This may occur because of the lower w/s, particle size distribution, differences in chemical composition, and the simultaneous formation of multiple hydration products. While bulk observations of the change in the high-absorption material are useful, investigation of individual particles could provide more insight into what is occurring.

3.1.2. Change of high-absorption material in individual particles

Single mC_3S and OPC particles were investigated to determine how particles of different sizes change over time. The particles were categorized into three diameter ranges between 8 μm and 60 μm. The number of individual particles investigated can be found in the Appendix. Particles smaller than 8 μm could not be measured reliably with the method in all time periods.

Fig. 4 shows the volume change of high-absorption materials of individual particles with respect to their volume in the first collected tomograph (70 min for mC_3S and 34 min for OPC). The absolute volume change was calculated by subtracting the volume of the particle at the target time period from the volume of the particle in the first measurement. The percentage change was calculated by normalizing the absolute volume change to the volume of the particle at first measurement. Each point shows the average volume change of the investigated particles. One standard error (SE) of the mean is also reported in the graphs. The standard error depends on both sample size and standard deviation and is used to calculate a confidence interval around the mean [58]. The variations for the larger particles are wide because there was a large

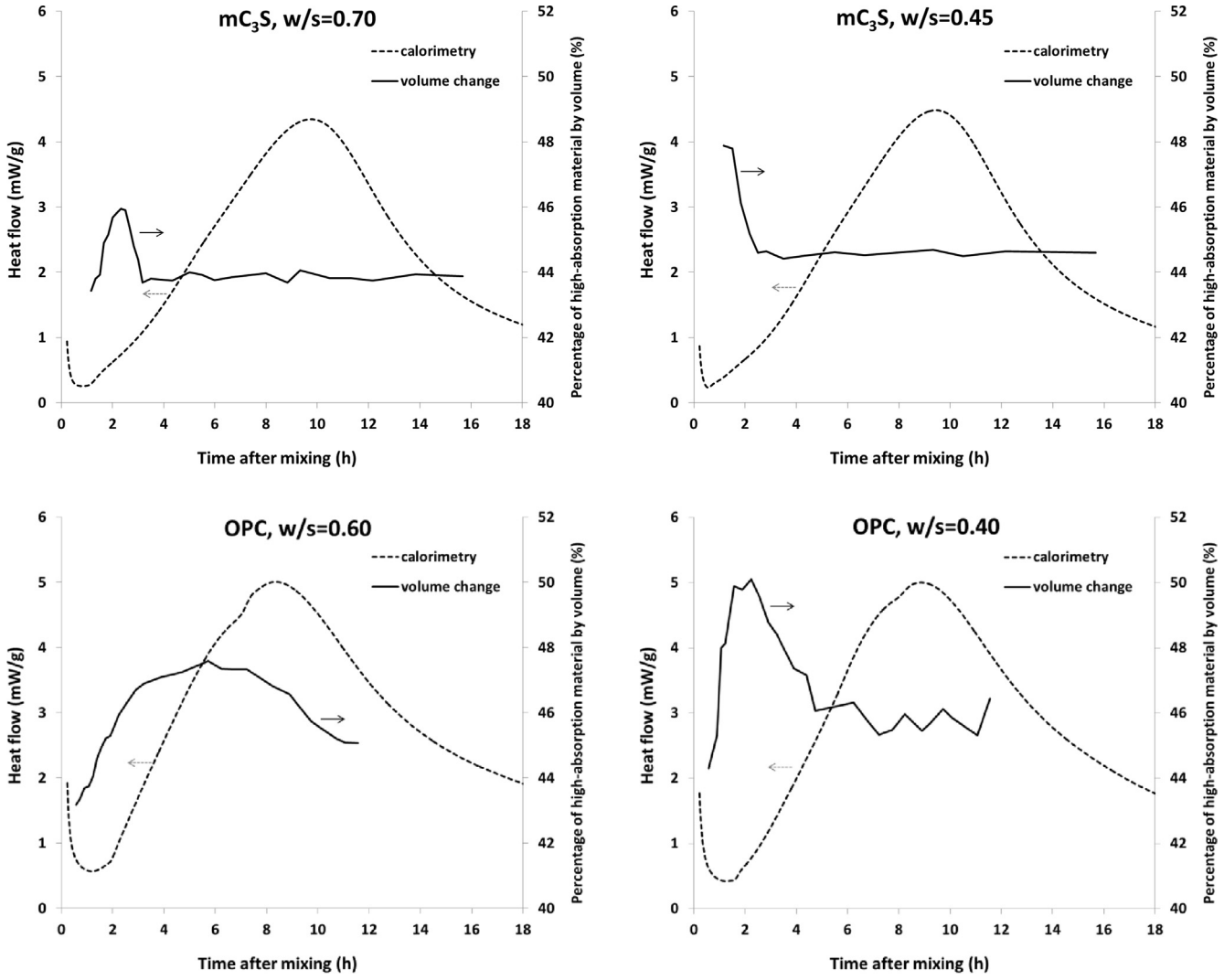

Fig. 3. Comparison of isothermal calorimetry to the volume change of high-absorption material from fCT (arrows in the graphs point to the corresponding Y-axis for each curve).

difference in the starting diameters of these particles. Despite this high variation, the averages show that there are distinct performances of different sized particles:

- All particles, except the smallest group in the OPC sample, had an increase in the volume of high-absorption materials followed by a decrease.
- The volume percentage change of high-absorption materials in smaller particles was higher than for the larger ones over the period of the test.
- The absolute volume of high-absorption materials in the larger particles changed more than smaller particles. This could be simply due to the fact that the quantity of large particles is more than the quantity of small particles.

The general performance of the individual particles was in accordance with the trends of the changes in total particle volume except that an initial increase in high-absorption volume was not observed in the smallest particles of OPC. It is possible that the initial increase in high-absorption occurred before the first collected data set.

After the initial volume change, the larger particles seem to have a negligible change in volume while the smaller particles are monotonically decreasing in volume. Since the smaller particles have a higher surface to volume ratio this would promote more rapid dissolution. On the other hand, the larger surface area of the larger particles make them more likely to serve as points of nucleation and therefore they appear to grow in size over the first three hours of hydration [59].

These results provide insights as to why the change in volume of high-absorption material can be almost constant while the calorimetry results suggest that there is a continued reaction. The particles that are smaller than 8 μm – which were not directly observed – are likely to continue to dissolve. Since the large particles account for the majority of the volume of the paste their behavior will govern the observed volume changes. Given that fCT can only observe the high-absorption material, these measurements do not provide a comprehensive picture of all hydration products. Nevertheless, these observations are useful in understanding the complex nature of hydration.

Three-dimensional reconstructions of three mC_3S particles at w/s = 0.70 in different size ranges are shown in Fig. 5. The volume of high-absorption material and average diameter are also reported. The particles are shown at the first measurement and then at different time periods that match critical times in hydration as suggested by the calorimetry curve. Regions that appear

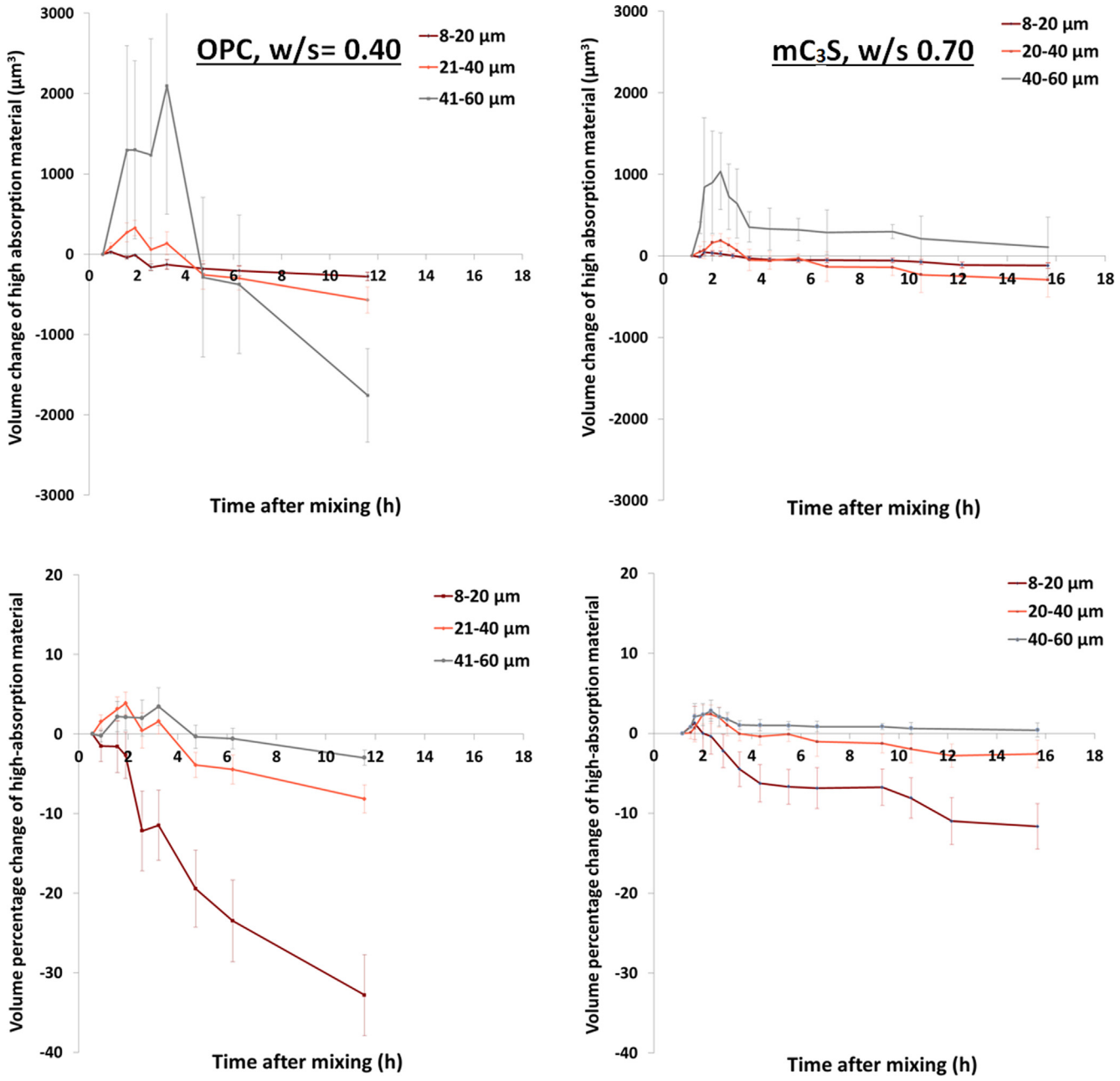

Fig. 4. Percentage and absolute volume change in individual high-absorption particles with respect to the initial volume at 34 min for OPC and 70 min for mC_3S pastes.

to have decreased X-ray absorption to where they would not be considered low absorption material are shown in green. These are regions where part of the anhydrous particle is no longer detected as high-absorption materials. This space may now be filled with fluid and/or low absorption hydration products. Regions that appear to have increased X-ray absorption are shown in dark gray.

Smaller high-absorption particles show more volume decrease and the larger particles show growth. The 3D renderings show that some regions near the surface of the anhydrous particles increase while others decrease in X-ray absorption. These regions of change seem to be found at only a few locations on the surface and do not occur uniformly. This could be attributed to enhanced reactivity at crystallographic defects or mechanical damage sites as suggested in other publications [8,13,44,60–64]. A recent study of hydration of C_3A particle showed non-uniformly reacted surface with the hydration products on surfaces varying in thickness up to 1 to 1.5 µm after 143 min of hydration in the presence of gypsum and water as observed by nCT at a voxel resolution of 20 nm [65].

3.2. Complementary experiments on individual particles

3.2.1. Microstructure observations by nCT

The nCT results for a collection of mC_3S particles are shown in Figs. 6 and 7 for hydration periods of 2 h and 10 h. These periods show the evolution of the microstructure from the induction period to the end of the acceleration period. The slice images from three different locations from both before and after hydration are labeled on the 3D reconstruction by dashed lines. The 3D reconstructions also show where hydration product has formed where it was not previously present.

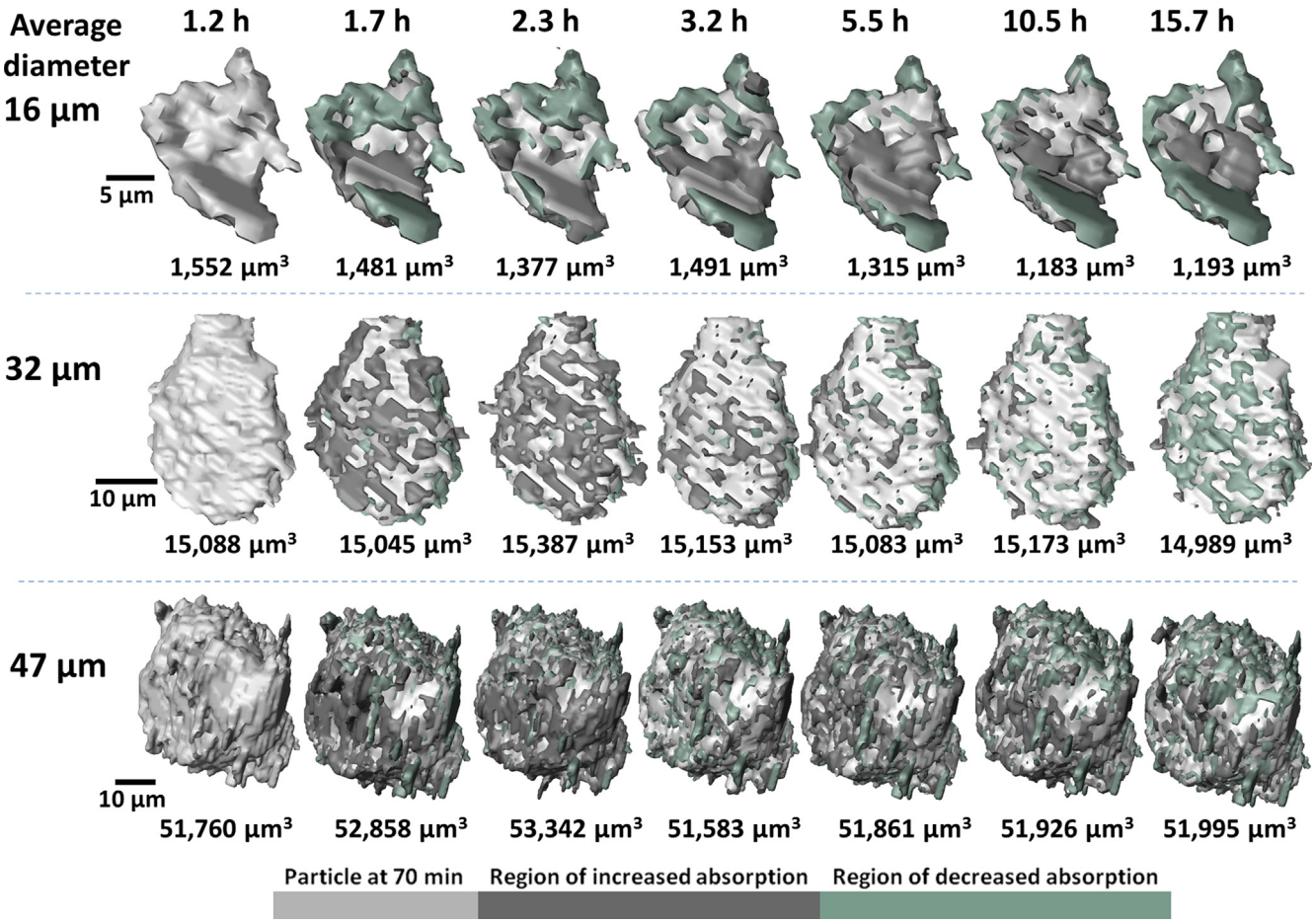

Fig. 5. Three Dimensional views of three mC_3S particles from different size ranges in critical time periods.

The sample that has hydrated for 2 h shows that hydration product forms directly on the surface of the particle and also extends over a micron away from the original particle. The hydration product that covers the surface of the anhydrous particle has a thickness between 60 and 100 nm. A product layer of this thickness would not be expected to be detected by the fCT experiments. However, the product that extends from the anhydrous particle surface could be detected. Furthermore, as particles hydrate in proximity to one another in lower w/s then this could create more extended product growth that would be detected. This has been observed in previous publication where collections of particles were observed in similar experiments [45].

The product occurs on only certain local regions of the particle surface while other regions remain almost unreacted. This non-uniform reaction of a pure anhydrous C_3S particle has been reported in previous publications to be caused by a high density of defects or differences in crystal structure [4,6–9,44].

After 10 h of hydration, the isolated regions of hydration product that were observed at 2 h are no longer present. Instead, the sample shows a high degree of reaction with a decrease in the anhydrous boundary by as much as 1 μm. This change in the anhydrous particle dimensions will contribute to the decrease in high-absorption material observed in the fCT data.

Although the overall volume of the particle shows an increase in size from the formation of hydration product, if these products are made up of a hydration product with a low X-ray absorption then this may explain why they are not observed in the fCT dataset. This interpretation is consistent with the observations of the individual particles in the fCT datasets shown in Fig. 4, where particles that range in size from 8 to 20 μm show a significant decrease in the volume of high-absorption material at the end of the acceleration period. This could be explained by changing chemical composition and/or structure over time. This will be addressed in more detail after discussing the chemical composition of the hydration products.

3.2.2. Observations of chemical composition

3.2.2.1. nXRF and nTACCo. The elemental maps for Ca, Si, $\bar{S}$ and Ca/Si from nXRF are shown in Fig. 8 and results from nTACCo are given in Table 3. The average density and one standard deviation are reported for [Ca], [Si], [$\bar{S}$], and molar Ca/Si. The maps at 2 h and 10 h are both normalized to the maximum value for each element in the figure. The volume of anhydrous mC_3S and hydration products, obtained from nCT dataset, is also included in Table 3. The chemical composition of the anhydrous samples from each time period is very similar, with a maximum difference in elemental density of 0.02 g/cm^3. This shows the reproducibility of the measurement.

For the sample hydrated for 2 h, the Ca/Si map shows that the hydration product was almost entirely above 4, and several locations were observed with a Ca/Si above 10. These regions with a Ca/Si above 10 are likely almost pure CH and were excluded from the averages in Table 3.

For the 10 h data, the Ca/Si of the hydration product is around 2 and there were no regions of Ca/Si above 10, but there is a region where the Ca/Si is above 4. The average Ca/Si is 2.3 for the hydration product and the sulfur density has decreased 5-fold when

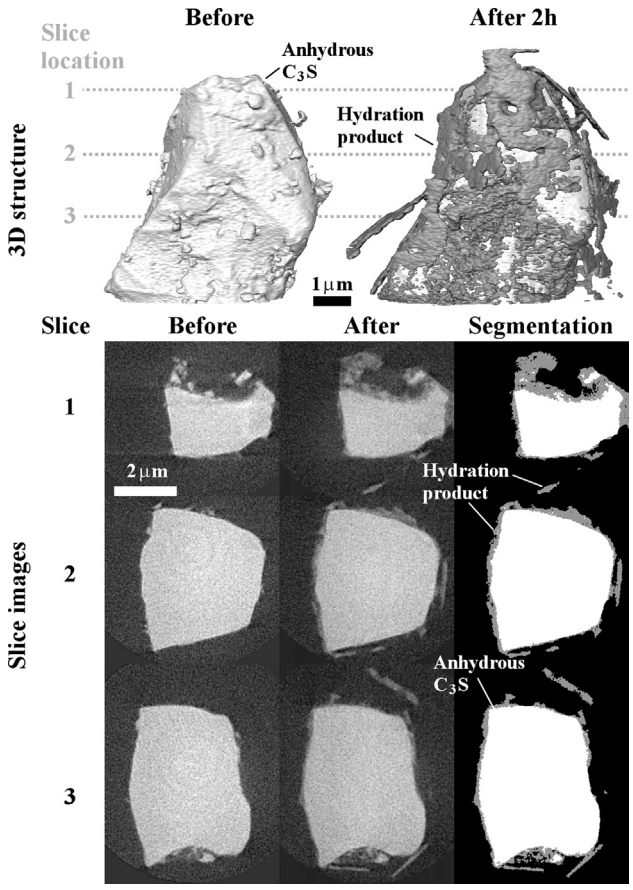

Fig. 6. The nCT dataset for an mC_3S particle showing the 3D structure and three different cross sections before and after 2 h of hydration in saturated lime + gypsum solution.

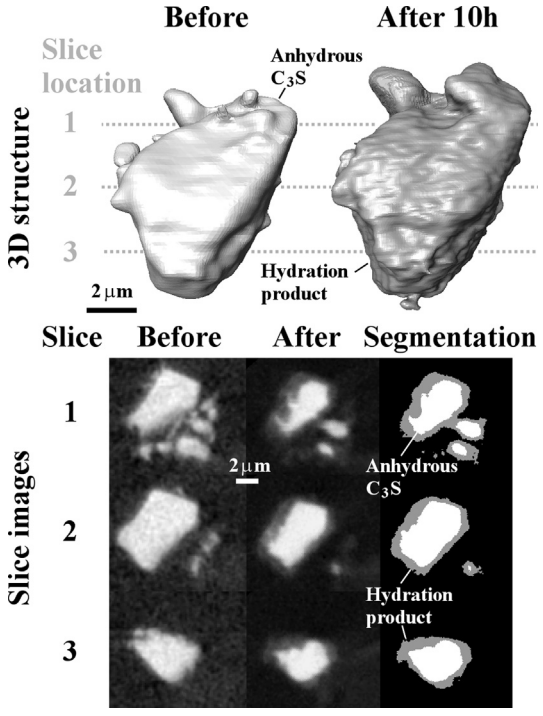

Fig. 7. The nCT dataset for an mC_3S particle showing the 3D structure and three different cross sections before and after 10 h of hydration in saturated lime + gypsum solution.

compared to the hydration product at 2 h. This suggests that the hydration product at 10 h could be mainly C-S-H with only local intermixing of CH.

The decrease in Ca/Si while Si remains almost constant in the hydration product from 2 h to 10 h is an important observation. One explanation is that the hydration product at 2 h contains soluble phases that are rich in [Ca] and [$\bar{S}$] (such as calcium hydroxide and calcium sulfate) that dissolve between 2 h and 10 h of hydration. This change in chemical composition is expected to alter the X-ray absorption of the material and this would change how the material is observed in the fCT experiments.

To further investigate this change in X-ray absorption, the mass attenuation coefficients for mixtures of C-S-H and CH with H/S between 1.2 and 4 and Ca/Si between 4 and 7.5 were calculated, and shown to produce an X-ray absorption similar to anhydrous C_3S. The details are included in the Appendix. Therefore, the hydration product formed at 2 h with Ca/Si = 4.40 ± 2.39 would be expected to have an X-ray absorption similar to C_3S. This could explain why this hydration product would cause an apparent growth in the high-absorption material measured by fCT. As Ca/Si is reduced to 2.3 ± 0.21 at 10 h, the X-ray mass attenuation coefficient of the hydration product would be between 20% and 27% lower than anhydrous C_3S and so it would be identified as low-absorption material in the fCT analysis.

3.2.2.2. SEM/EDS investigation. Analysis with SEM-EDS was used to provide a measurement of the chemical composition of the surface materials. The method was first used to make repeated measurements on the surface of the anhydrous OPC and mC_3S particles to examine the repeatability of the method and determine an initial chemical composition at the surface. A repeat measurement of anhydrous OPC was completed for two samples and the individual measurements show less than 1% difference for the mean and standard error in all measurements except Al showed a 1.9% difference in the mean. The differences in [Al] could be caused by different amounts of C_3A and C_4AF in the analyzed material. This shows that the method is repeatable.

Next several OPC and mC_3S particles were investigated both before and after hydration for 5, 10, 20, and 36 min in 15 mM lime solution with w/s = 10. As described in the Methods, the samples were carefully aligned before and after the reaction to measure the chemical composition changes. The normalized mass percentage of Ca, Si, O, Fe, and Al before and after hydration can be found in the Appendix. The molar Ca/Si ratio is used to provide additional insight and allow comparison with other measurements. This ratio may be more accurate than the separate elemental contents, because this technique uses normalized elemental content and not actual concentrations. The average variation of Ca/Si between two repeat measurements of anhydrous materials was 0.1.

Fig. 9 shows the change in Ca/Si in different testing conditions. One standard error is also reported on the curves. The figure shows that the Ca/Si of the anhydrous samples were close to 3.0 as expected. The OPC particles hydrated for 5 min show that the Ca/Si changed from 2.8 to 3.5, which could represent the initial formation of hydration products. The Ca/Si in mC_3S particles did not change considerably after 5 min. This may reflect the higher reactivity of OPC compared to mC_3S as observed by the calorimetry curves and volume change in fCT data from Fig. 3.

In each system, the measured Ca/Si increased until 20 min and then started to decrease. At 20 min there was an increase in Ca/Si of 36% and 19% for OPC and mC_3S, respectively, which is greater than the standard error. Further investigation suggests that [Ca] seems to be increasing while [Si] is almost constant. This could mean that these materials are a mixture of C-S-H and CH with a larger amount of CH or possibly another hydration product that

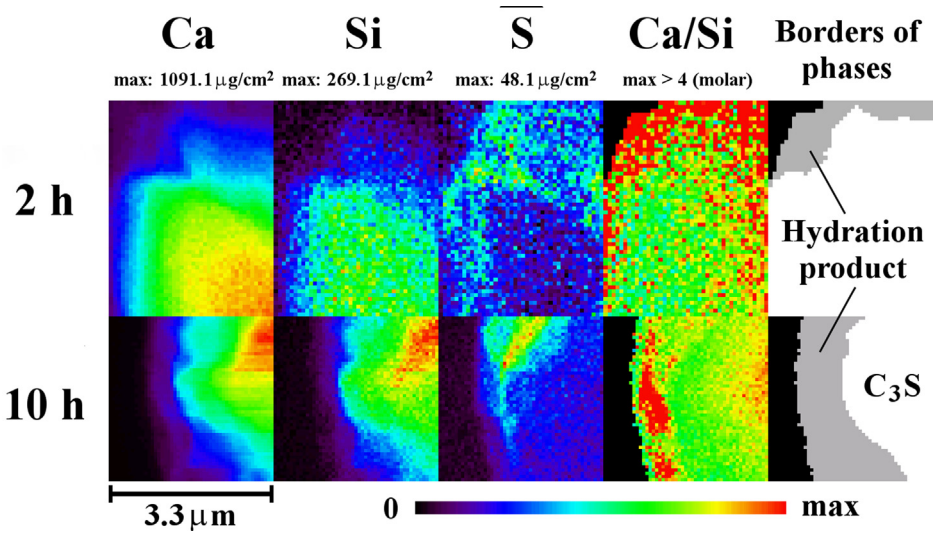

Fig. 8. The elemental maps from nXRF analysis after 2 h and 10 h of hydration for mC_3S of particles from Figs. 6 and 7. An image at the right from nCT results shows the boundary between the hydration product and the anhydrous region. The maps are both normalized to the maximum value for each element in the figure.

Table 3
The elemental density, Ca/Si ratio from the nTACCo analysis, and phase volume obtained from nCT for mC_3S after 2 h and 10 h of hydration. Points with excessive values (Ca/Si > 10) are excluded as they are likely CH.

		Anhydrous C_3S		Hydration product	
		2 h	10 h	2 h	10 h
Ca (g/cm^3)		1.69 ± 0.06	1.68 ± 0.19	1.12 ± 0.54	0.47 ± 0.19
Si (g/cm^3)		0.40 ± 0.08	0.42 ± 0.06	0.20 ± 0.17	0.14 ± 0.08
$\bar{S}$(g/cm^3)		0.028 ± 0.013	0.01 ± 0.013	0.173 ± 0.093	0.037 ± 0.027
Ca/Si (molar)		3.08 ± 0.64	2.77 ± 0.08	4.40 ± 2.39	2.31 ± 0.21
Volume (μm^3)	before hydration	66.03	225.61	–	–
	after hydration	61.67	117.20	10.62	106.24

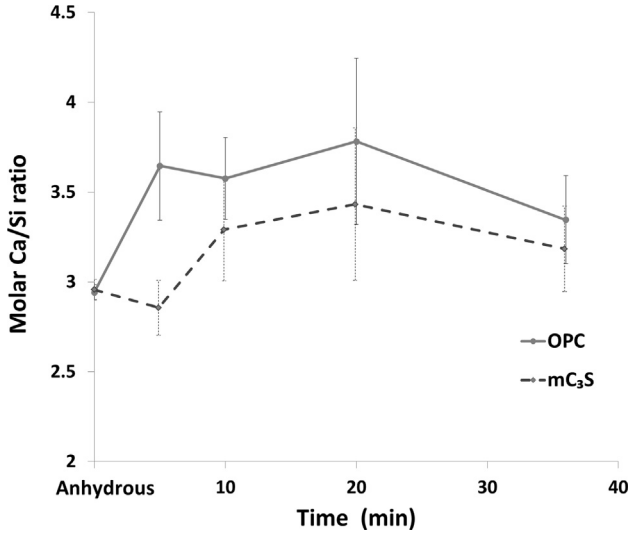

Fig. 9. The molar Ca/Si for different time periods after hydration for a collection of OPC and mC_3S particles in saturated lime water with w/s = 10 as measured by SEM/EDS.

is rich in Ca. After 36 min of hydration, both materials showed a decrease of 10% and 6% with respect to 20 min in Ca/Si of OPC and mC_3S samples, respectively. Again, this seems to be a change in the amount of Ca in the material as [Si] does not change significantly. The change of the Ca/Si shows the same pattern as the percentage of high-absorption materials in fCT data.

Care has to be taken in interpreting these results, because the samples were not polished or coated, to avoid introducing artifacts to the fragile samples. Furthermore, the interaction volume of the electron beam could consist of a mixture of the hydration product and an unknown proportion of anhydrous C_3S. However, an agreement has been found for SEM-EDS on materials of similar age and nXRF for early age hydration products [45]. Unfortunately, there are very few techniques that are capable of measuring the surface chemical composition of samples at this early point of reaction.

4. Discussion

4.1. Change in high-absorption material

Based on the results from four different imaging techniques at multiple length scales with different solution environments, it appears that the hydration products formed within the first few hours have a different average chemical composition than the hydration products after 10 h. The results show that the chemical composition of these materials are different enough that they will increase the local X-ray absorption and these changes can be observed in fCT.

Measurements with fCT of over 60,000 particles for multiple systems and w/s have been used to investigate this change in X-ray absorption. The results show that the volume of the high-absorption material increases during the induction period until a maximum value is reached near the start of the acceleration period. Based on the SEM-EDS and nTACCo results the increase in high absorption materials appears to be caused by the formation of

hydration products that are rich in CH and $C\bar{S}$ with an average Ca/Si > 4.

The changes of individual high-absorption particles from fCT show that particles smaller than 20 μm decrease in size with time while the larger particles increase in size. This decrease in particle size is caused by a higher amount of dissolution than the formation of hydration products. This same process may be happening on all particles, but the smaller particles may show these changes to a greater degree, because of the larger density of defects and/or their higher surface area to volume ratio and therefore higher reactivity of the smaller particles [61,66].

One important observation in the particles larger than 20 μm is that the amount of high-absorption material increases until the beginning of the acceleration period and then decreases. The nXRF and nTACCo results suggest that the Ca and $\bar{S}$ concentration in the hydration products is greater at 2 h of hydration than at 10 h. In fact, the Ca/Si at 10 h is 2.3 compared to 4.40 at 2 h of hydration. These changes in chemical composition and density may cause the X-ray absorption to decrease, which decreases the contrast in the fCT data and consequently reduces the detected amount of high-absorption material.

4.2. Insights into the cause of the induction and acceleration period

Based on the findings from this work and others [10,12,31,44,45] important insights are provided into hydration. Conceptual images of this process are included in Fig. 10 to accompany the explanation.

Anhydrous C_3S has surfaces with different levels of reactivity as shown in Fig. 10a. When these reactive regions are exposed to the solution they will cause etch pits on the surface of the reacting grains as shown in Fig. 10b [4–6,8]. The smaller particles may have a higher density (quantity-of-defects/volume) of these regions and this could cause their rapid dissolution as shown with fCT results in this paper. This could also be caused by smaller particles having a higher number of exposed lattice plane edges that would initiate dissolution [67,68].

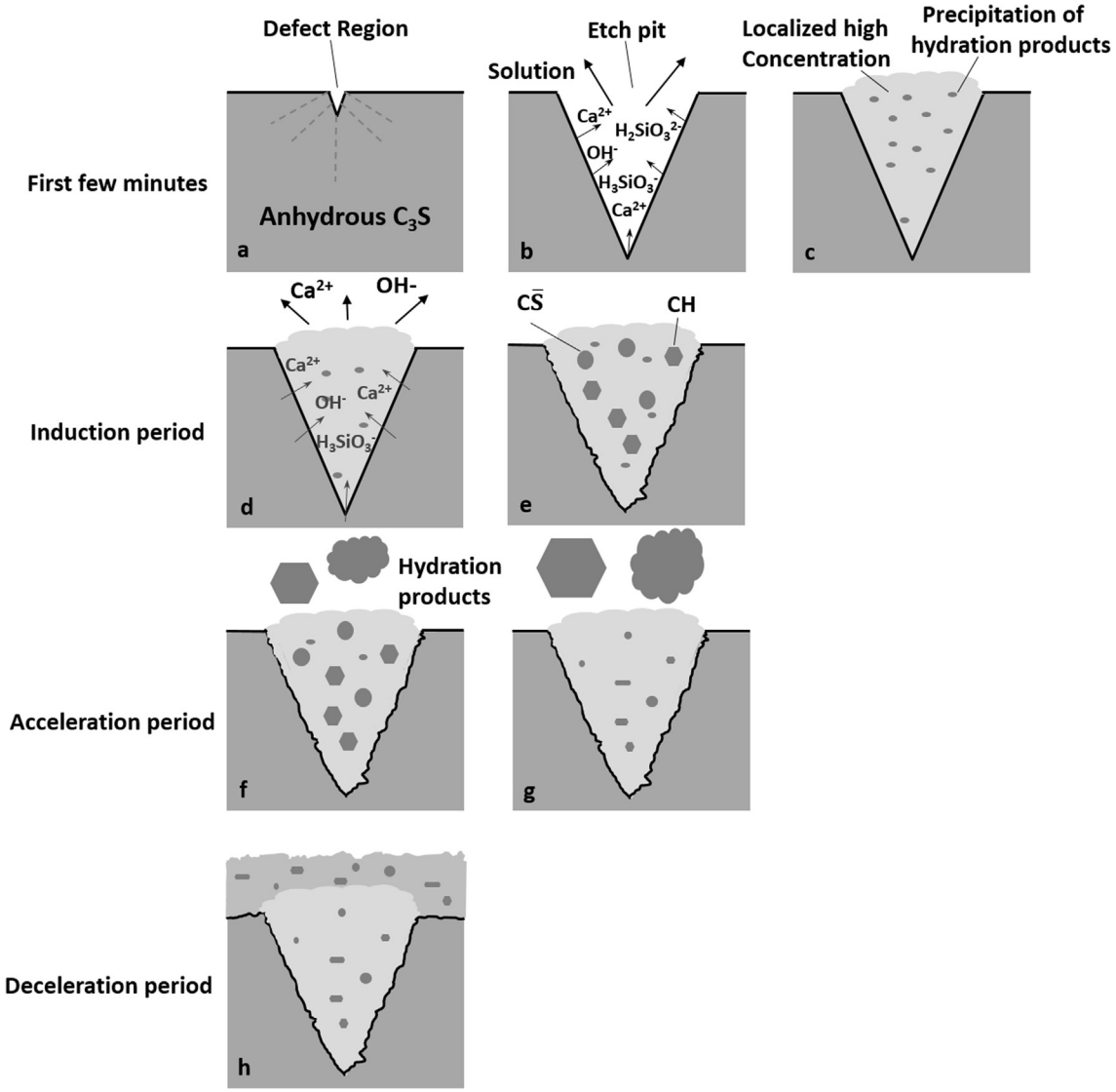

Fig. 10. Schematic demonstration of the proposed mechanism; a) region of defect on anhydrous cement particle, b) formation of etch pit with high ionic concentration within, c) increased ionic concentration within the pit and formation of hydration products, d) the region of defect continues to react but at a reduced rate and local ion concentration increases within the pit, e) ion concentration increase continues and CH and CS precipitate within the pores of the C-$\bar{S}$-H, f) ion concentration builds in solution until hydration products form in the bulk solution, g) the hydration product formation in the bulk solution causes the CH and CS precipitates to dissolve and modifies the surface of the more slowly reacting surface of the anhydrous particle, h) surface of particle is covered by hydration products and this slows dissolution.

Because of the pit geometry, the ion concentration may become high enough that hydration products start forming within the pit as shown in Fig. 10c. Experiments investigating hydration of triclinic C_3S with nTACCo in w/s = 5 have found C-S-H with Ca/Si = 1.53 and 1.68 and a mass density of 1.34 and 1.69 g/cm^3 filling these pits during the induction period [44]. This density and chemistry of the C-S-H match the measurements for inner product C-S-H that is several months old [69,70]. These reacted regions were found in ≈ 34% of the volume of the particles investigated with volumes between 17 μm^3 and 98 μm^3 at 2 h of hydration. This is a significant amount of material that has dissolved. The ions will cause the formation of hydration products and increase the ion concentration in the bulk solution.

The C-S-H formed in the pit will decrease the access of solution to the fast reacting surfaces and this will slow the rate of reaction. As the reactive surface continues to react, it will continue to release ions that will be forced to travel through the C-S-H to escape the pit. As this process continues the local ionic concentration within the pit will increase (Fig. 10d). Once the concentration is high enough this will cause precipitates such as CH and $C\bar{S}$ to form within the pores of the C-S-H (Fig. 10e). Since these pores are expected to be fine, these precipitates may be only a few nanometers in size. Fig. 8 shows observations of localized concentrations of CH and $C\bar{S}$ at 2 h of hydration (i.e., during the induction period). Once these precipitates form they increase the X-ray absorption of the hydration products. This is why the fCT shows an increase in the high-absorption material.

The ionic concentration of Ca in the pore solution increases during the induction period until hydration products start forming in the bulk solution [10,12] as shown in Fig. 10f. Since these precipitates are not constrained they will be much larger than the nano CH and $C\bar{S}$. Because of the large size difference, the smaller crystals are expected to dissolve while the larger precipitates grow through Ostwald ripening.

The 10 h nTACCo results show that the hydration product has a Ca/Si ≈ 2.3 ± 0.21, which is much lower than the Ca/Si ≈ 4.4 ± 2.39 at 2 h. This supports the idea that the chemical composition of the hydration product is changing and lowering the X-ray absorption. This reduction in X-ray absorption supports the changes in high-absorption material observed by fCT in Fig. 2.

After 10 h of hydration, it appears that there is dissolution of all regions on the surface of the C_3S particle. While the observations in this paper do not reveal why surfaces change their reactivity during the acceleration period, one possible explanation is that the slowly reacting regions may be hydroxylated or covered with a hydration product such as a metastable layer [2,13,71–73]. The drop in the ionic concentration at the start of the acceleration period may disturb this layer and allow all surfaces to begin reacting. More work is needed to better understand this.

Another observation made at 10 h is that the particle surface is covered in hydration products (Fig. 10h). These products may reduce the availability of the solution to the surface and then slow the dissolution and therefore the reaction of the surface. This may be responsible for the deceleration period. Others have suggested that reactive surfaces may be obscured by hydration products [1–3].

This interpretation of the measurements gives insights into a plausible explanation for the onset of the induction period, followed by rapid cement dissolution during the acceleration period, and later by the slowing of reaction during the deceleration period. This interpretation is based on observations using several X-ray imaging methods to measure the structure and chemical composition of the hydration products. It suggests that a detailed understanding of both composition and structural changes is needed to accurately describe these phenomena. Additional work is underway to make a larger number of observations as well as nanoscale in-situ measurements of these critical periods. Ultimately this work will be useful to build mechanistic numerical models that can more accurately predict the behavior of hydrating cement systems. This could also be used to provide new insights into admixture design and manufacturing processes of cement to improve performance.

5. Conclusions

This paper provides observations of the evolution of OPC and mC_3S during hydration over the first 16 h by using four different imaging methods. A strength of the current study is the use of fCT to observe 3D changes of roughly 60,000 particles at 1 μm voxel size. These observations are then supported by nanoscale observations in dilute solutions with nCT. Quantitative measurements of the chemical composition and structure at the nanoscale were made by nTACCo. The following conclusions can be drawn:

- Micron-scale measurements show that the volume of the high X-ray absorption material increases during the induction period and seems to form on the surface of the particles >20 μm, while the particles smaller than 20 μm show primarily dissolution. These same measurements show that as the acceleration period begins the X-ray absorption of the hydration product decreases.
- Nanoscale measurements during the induction period for 2 h of hydration in a saturated lime + gypsum solution found an average Ca/Si of 4.4 (±2.39), while the same measurements on particles after 10 h of hydration found an average Ca/Si of 2.31 (±0.21).
- After 2 h of hydration, some regions have Ca/Si > 10 which are likely to contain CH and phases with high $\bar{S}$ content.
- Both the nano and micron scale measurements show non-uniform growth and dissolution on the surface of the reacting particles. The nanoscale measurements show that at 2 h of hydration the hydration products extend only a few microns away from the particle surface.

This work provides novel observations into the formation and subsequent change in chemical composition of early age hydration products. Based on these observations several mechanisms are suggested that could control the induction and acceleration period in cement hydration. This work shows the value of combining time-resolved imaging at different length scales and the insights that they can provide on complicated physical and chemical processes.

Conflict of interest

None.

Acknowledgment

This work was sponsored by funding from Federal Highway Administration (FHWA) Exploratory Advanced Research (EAR) program and funding from the United State National Science Foundation CMMI 1150404 CAREER Award. We thank our collaborators, Brad Chmelka (University of California, Santa Barbara), Andreas Lüttge and Rolf Arvidson (University of Bremen), Denise Silva and Josephine Cheung (GCP Applied Technologies), and Larry Robert (Roberts Consulting), for their insightful advice on this work. A special thanks are also given to Narges Nourian for all of her help on with the data analysis. The XRD measurements were made at GCP by Jeffrey Nicolich.

Use of the Center for Nanoscale Materials and the Advanced Photon Source, both Office of Science user facilities, was supported by the U.S. Department of Energy, Office of Science, Office of Basic Energy Sciences, under Contract No. DE-AC02-06CH11357.

Appendix A. Supplementary data

Supplementary data to this article can be found online at https://doi.org/10.1016/j.conbuildmat.2019.04.013.

References

[1] J.G.M. Dejong, H.N. Stein, J.M. Stevels, Hydration of tricalcium silicate, J. Appl. Chem. 17 (9) (1967) 246–250.
[2] H.M. Jennings, P.L. Pratt, Experimental argument for the existence of a protective membrane surrounding portland-cement during the induction period, Cem. Concr. Res. 9 (4) (1979) 501–506.
[3] H.N. Stein, J.M. Stevels, Influence of silica on hydration of 3cao, Sio2, J. Appl. Chem. 14 (8) (1964) 338.
[4] P. Juilland, E. Gallucci, Morpho-topological the mechanisms and kinetic regimes of alite dissolution, Cem. Concr. Res. 76 (2015) 180–191.
[5] K.L. Scrivener, P. Juilland, P.J.M. Monteiro, Advances in understanding hydration of Portland cement, Cem. Concr. Res. 78 (2015) 38–56.
[6] J.W. Bullard, G.W. Scherer, J.J. Thomas, Time dependent driving forces and the kinetics of tricalcium silicate hydration, Cem. Concr. Res. 74 (2015) 26–34.
[7] F. Bellmann, T. Sowoidnich, H.M. Ludwig, D. Damidot, Dissolution rates during the early hydration of tricalcium silicate, Cem. Concr. Res. 72 (2015) 108–116.
[8] P. Juilland, E. Gallucci, R. Flatt, K. Scrivener, Dissolution theory applied to the induction period in alite hydration, Cem. Concr. Res. 40 (6) (2010) 831–844.
[9] L. Nicoleau, M.A. Bertolim, Analytical model for the alite (C3S) dissolution topography, J. Am. Ceram. Soc. 99 (3) (2016) 773–786.
[10] P.W. Brown, E. Franz, G. Frohnsdorff, H.F.W. Taylor, Analyses of the aqueous phase during early C3s hydration, Cem. Concr. Res. 14 (2) (1984) 257–262.
[11] K.L. Scrivener, A. Nonat, Hydration of cementitious materials, present and future, Cem. Concr. Res. 41 (7) (2011) 651–665.
[12] J.F. Young, H.S. Tong, R.L. Berger, Compositions of solutions in contact with hydrating tricalcium silicate pastes, J. Am. Ceram. Soc. 60 (5–6) (1977) 193–198.
[13] J.W. Bullard, H.M. Jennings, R.A. Livingston, A. Nonat, G.W. Scherer, J.S. Schweitzer, K.L. Scrivener, J.J. Thomas, Mechanisms of cement hydration, Cem. Concr. Res. 41 (12) (2011) 1208–1223.
[14] D.H.C. Harris, C.G. Windsor, C.D. Lawrence, Free and bound water in cement pastes, Mag. Concr. Res. 26 (87) (1974) 65–72.
[15] B. Lothenbach, F. Winnefeld, C. Alder, E. Wieland, P. Lunk, Effect of temperature on the pore solution, microstructure and hydration products of Portland cement pastes, Cem. Concr. Res. 37 (4) (2007) 483–491.
[16] I. Pane, W. Hansen, Investigation of blended cement hydration by isothermal calorimetry and thermal analysis, Cem. Concr. Res. 35 (6) (2005) 1155–1164.
[17] X.Y. Pang, P. Boul, W.C. Jimenez, Isothermal calorimetry study of the effect of chloride accelerators on the hydration kinetics of oil well cement, Constr. Build. Mater. 77 (2015) 260–269.
[18] J. Stark, Recent advances in the field of cement hydration and microstructure analysis, Cem. Concr. Res. 41 (7) (2011) 666–678.
[19] J. Bensted, Some applications of conduction calorimetry to cement hydration, Adv. Cem. Res. 1 (1987) 35–44.
[20] M.D. Andersen, H.J. Jakobsen, J. Skibsted, Characterization of white Portland cement hydration and the C-S-H structure in the presence of sodium aluminate by Al-27 and Si-29 MAS NMR spectroscopy, Cem. Concr. Res. 34 (5) (2004) 857–868.
[21] E.T. Rodriguez, I.G. Richardson, L. Black, E. Boehm-Courjault, A. Nonat, J. Skibsted, Composition, silicate anion structure and morphology of calcium silicate hydrates (C-S-H) synthesised by silica-lime reaction and by controlled hydration of tricalcium silicate (C3S), Adv. Appl. Ceram. 114 (7) (2015) 362–371.
[22] T. Sowoidnich, F. Bellmann, D. Damidot, H.M. Ludwig, New insights into tricalcium silicate hydration in paste, J. Am. Ceram. Soc. 102 (5) (2019) 2965–2976.
[23] A. Bazzoni, M. Cantoni, K.L. Scrivener, Impact of annealing on the early hydration of tricalcium silicate, J. Am. Ceram. Soc. 97 (2) (2014) 584–591.
[24] K.O. Kjellsen, H. Justnes, Revisiting the microstructure of hydrated tricalcium silicate – a comparison to Portland cement, Cem. Concr. Comput. 26 (8) (2004) 947–956.
[25] K.O. Kjellsen, B. Lagerblad, Microstructure of tricalcium silicate and Portland cement systems at middle periods of hydration-development of Hadley grains, Cem. Concr. Res. 37 (1) (2007) 13–20.
[26] D. Menetrier, I. Jawed, T.S. Sun, J. Skalny, Esca and Sem Studies on Early C3s Hydration, Cem. Concr. Res. 9 (4) (1979) 473–482.
[27] G.W. Groves, Portland-cement clinker viewed by transmission electron-microscopy, J. Mater. Sci. 16 (4) (1981) 1063–1070.
[28] P.J.M. Monteiro, S.J. Bastacky, T.L. Hayes, Low-temperature scanning electron-microscope analysis of the portland-cement paste early hydration, Cem. Concr. Res. 15 (4) (1985) 687–693.
[29] D.M.F. Orr, Application of the scanning electron-microscope to the study of the initial hydration of portland-cement paste, Cem. Concr. Res. 13 (1) (1983) 146–148.
[30] L. Zhang, G.W. Scherer, Comparison of methods for arresting hydration of cement, Cem. Concr. Res. 41 (10) (2011) 1024–1036.
[31] J.B. Ings, P.W. Brown, G. Frohnsdorff, Early hydration of large single-crystals of tricalcium silicate, Cem. Concr. Res. 13 (6) (1983) 843–848.
[32] J.W. Bullard, R.J. Flatt, New insights into the effect of calcium hydroxide precipitation on the kinetics of tricalcium silicate hydration, J. Am. Ceram. Soc. 93 (7) (2010) 1894–1903.
[33] S. Garrault, E. Finot, E. Lesniewska, A. Nonat, Study of C-S-H growth on C3S surface during its early hydration, Mater. Struct. 38 (278) (2005) 435–442.
[34] M.C.G. Juenger, P.J.M. Monteiro, E.M. Gartner, G.P. Denbeaux, Soft X-ray microscope investigation into the effects of calcium chloride on tricalcium silicate hydration, Cem. Concr. Res. 35 (1) (2005) 19–25.
[35] E.E. Bernardes, E.V.M. Carrasco, W.L. Vasconcelos, A.G. de Magalhaes, X-ray microtomography (mu-CT) to analyze the pore structure of a Portland cement composite based on the selection of different regions of interest, Constr. Build. Mater. 95 (2015) 703–709.
[36] T.J. Chotard, M.P. Boncoeur-Martel, A. Smith, J.P. Dupuy, C. Gault, Application of X-ray computed tomography to characterise the early hydration of calcium aluminate cement, Cem. Concr. Comput. 25 (1) (2003) 145–152.
[37] Q. Hu, M. Aboustait, M.T. Ley, J.C. Hanan, V. Rose, R. Winarski, Combined three-dimensional structure and chemistry imaging with nanoscale resolution, Acta Mater. 77 (2014) 173–182.
[38] M. Moradian, Direct Observations on Microstructure Evolution of Cement Systems at Early Ages, State University, Oklahoma, 2017.
[39] M. Moradian, Q. Hu, M. Aboustait, M.T. Ley, J.C. Hanan, X. Xiao, G.W. Scherer, Z. Zhang, Direct observation of void evolution during cement hydration, Mater. Des. 136 (2017) 137–149.
[40] M. Moradian, M.T. Ley, Z.C. Grasley, Stress induced dissolution and time-dependent deformation of portland cement paste, Mater. Des. 157 (2018) 314–325.
[41] M. Ley, Q. Hu, M. Aboustait, T. Kim, M. Moradian, J. Hanan, V. Rose, R. Winarski, J. Gelb, Combining Nano X-ray Tomography and Nano X-ray Fluorescence to Create Time-dependent Three Dimensional Constitutive Maps, 2015.
[42] G. Sokhansefat, M.T. Ley, M.D. Cook, R. Alturki, M. Moradian, Investigation of concrete workability through characterization of aggregate gradation in hardened concrete using X-ray computed tomography, Cem. Concr. Compos. 98 (2019) 150–161.
[43] G. Sokhansefat, Feature Investigation using Micro Computed Tomography within Materials, Oklahoma State University, Stillwater, OK, 2018.
[44] Q. Hu, M. Aboustait, T. Kim, M.T. Ley, J. Bullard, G. Scherer, J.C. Hanan, V. Rose, R. Winarski, J. Gelb, Direct measurements of 3d structure, chemistry and mass density during the induction period of C3s hydration, Cem. Concr. Res. 89 (2016) 14–26.
[45] Q. Hu, M. Aboustait, T. Kim, M.T. Ley, J.C. Hanan, J.W. Bullard, R. Winarski, V. Rose, Direct three-dimensional observation of the microstructure and chemistry of C3S hydration, Cem. Concr. Res. 88 (2016) 157–169.
[46] J.J. Williams, Z. Flom, A.A. Amell, N. Chawla, X. Xiao, F. De Carlo, Damage evolution in SiC particle reinforced Al alloy matrix composites by X-ray synchrotron tomography, Acta Mater. 58 (18) (2010) 6194–6205.
[47] X.D. Zhang, C.J. Xia, X.H. Xiao, Y.J. Wang, Fast synchrotron X-ray tomography study of the packing structures of rods with different aspect ratios, Chinese Phys B 23 (4) (2014).
[48] M. Holt, R. Harder, R. Winarski, V. Rose, Nanoscale hard X-Ray microscopy methods for materials studies, Annu. Rev. Mater. Res. 43 (2013) 183–211.
[49] N.D. Parab, B. Claus, M.C. Hudspeth, J.T. Black, A. Mondal, J.Z. Sun, K. Fezzaa, X.H. Xiao, S.N. Luo, W.N. Chen, Experimental assessment of fracture of individual sand particles at different loading rates, Int. J. Impact Eng. 68 (2014) 8–14.
[50] F. De Carlo, P.B. Albee, Y.S. Chu, D.C. Mancini, B. Tieman, S.Y. Wang, High-throughput real-time X-ray microtomography at the advanced photon source, in: International Symposium on Optical Science and Technology, International Society for Optics and Photonics, 2002, pp. 1–13.
[51] F. De Carlo, B. Tieman, High-throughput X-ray microtomography system at the advanced photon source beamline 2-BM, in: In Optical Science and Technology, the SPIE 49th Annual Meeting, International Society for Optics and Photonics, 2004, pp. 644–651.
[52] J.W. Bullard, B. Lothenbach, P.E. Stutzman, K.A. Snyder, Coupling thermodynamics and digital image models to simulate hydration and microstructure development of portland cement pastes, J. Mater. Res. 26 (4) (2011) 609–622.
[53] T. Kim, M. Moradian, M.T. Ley, Dissolution and leaching of fly ash in nitric acid using automated scanning electron microscopy, Adv. Civ. Eng. Mater. 7 (1) (2018) 291–307.
[54] F.R. Brushett, L. Trahey, X.H. Xiao, J.T. Vaughey, Full-field synchrotron tomography of nongraphitic foam and laminate anodes for lithium-ion batteries, ACS Appl. Mater. Inter. 6 (6) (2014) 4524–4534.
[55] A. Momose, T. Takeda, Y. Itai, K. Hirano, Phase-contrast X-ray computed tomography for observing biological soft tissues (vol 2, pg 473, 1996), Nat. Med. 2 (5) (1996). 596 596.
[56] D. Damidot, A. Nonat, P. Barret, Kinetics of tricalcium silicate hydration in diluted suspensions by microcalorimetric measurements, J. Am. Ceram. Soc. 73 (11) (1990) 3319–3322.

[57] R.P. Winarski, M.V. Holt, V. Rose, P. Fuesz, D. Carbaugh, C. Benson, D.M. Shu, D. Kline, G.B. Stephenson, I. McNulty, J. Maser, A hard X-ray nanoprobe beamline for nanoscale microscopy, J. Synchrotron Radiat. 19 (2012) 1056–1060.
[58] D.G. Altman, J.M. Bland, Statistics notes – standard deviations and standard errors, Brit Med J 331 (7521) (2005). 903 903.
[59] S. Garrault, T. Behr, A. Nonat, Formation of the C-S-H layer during early hydration of tricalcium silicate grains with different sizes, J. Phys. Chem. B 110 (1) (2006) 270–275.
[60] J.N. Maycock, J. Skalny, R. Kalyoncu, Crystal defects and hydration I. Influence of lattice defects, Cem. Concr. Res. 4 (1974) 835–847.
[61] L. Nicoleau, A. Nonat, D. Perrey, The di- and tricalcium silicate dissolutions, Cem. Concr. Res. 47 (2013) 14–30.
[62] I. Odler, H. Dorr, Early hydration of tricalcium silicate. 2. Induction period, Cem. Concr. Res. 9 (3) (1979) 277–284.
[63] I. Odler, J. Schuppstuhl, Early hydration of tricalcium silicate. 3. Control of the induction period, Cem. Concr. Res. 11 (5–6) (1981) 765–774.
[64] T. Sakurai, T. Sato, A. Yoshinaga, The effect of minor components on the early hydraulic activity of the major phases of Portland cement clinker, 5th ISCC (1969) 300-321.
[65] G. Geng, R.J. Myers, Y.-S. Yu, D.A. Shapiro, R. Winarski, P.E. Levitz, D.A. Kilcoyne, P.J. Monteiro, Synchrotron X-ray nanotomographic and spectromicroscopic study of the tricalcium aluminate hydration in the presence of gypsum, Cem. Concr. Res. (2018).
[66] A. Navrotsky, Nanoscale effects on thermodynamics and phase equilibria in oxide systems, ChemPhysChem 12 (12) (2011) 2207–2215.
[67] L. Briese, R.S. Arvidson, A. Luttge, The effect of crystal size variation on the rate of dissolution–A kinetic Monte Carlo study, Geochim. Cosmochim. Acta 212 (2017) 167–175.
[68] M. Petrik, B. Harbrecht, Dissolution Kinetics of Nanocrystals, ChemPhysChem 14 (11) (2013) 2403–2406.
[69] I.G. Richardson, The nature of C-S-H in hardened cements, Cem. Concr. Res. 29 (8) (1999) 1131–1147.
[70] E. Gallucci, P. Mathur, K. Scrivener, Microstructural development of early age hydration shells around cement grains, Cem. Concr. Res. 40 (1) (2010) 4–13.
[71] E.M. Gartner, A proposed mechanism for the growth of C-S-H during the hydration of tricalcium silicate, Cem. Concr. Res. 27 (5) (1997) 665–672.
[72] E.M. Gartner, J.M. Gaidis, Hydration mechanisms: I, Mater. Sci. Concr. III I (1) (1989) 95.
[73] E. Gartner, I. Maruyama, J. Chen, A new model for the CSH phase formed during the hydration of Portland cements, Cem. Concr. Res. 97 (2017) 95–106.